

Pulsed Growth of Vertically Aligned Nanotube Arrays with Variable Density

Jeremy J. Jackson,[†] Alex A. Puretzky,[†] Karren L. More,[‡] Christopher M. Rouleau,[†] Gyula Eres,[‡] and David B. Geohegan^{†,*}

[†]Center for Nanophase Materials Sciences and [‡]Materials Science and Technology Division, Oak Ridge National Laboratory, Oak Ridge, Tennessee 37831-6488, United States

Among the wide variety of carbon nanotube composite architectures,^{1–3} vertically aligned nanotube arrays (VANTAs) attract special attention since they self-assemble during growth into dense, self-supporting, oriented arrays that can be grown to centimeter lengths.⁴ The VANTA platform of vertically oriented, continuous nanotubes is highly promising for a wide range of different applications such as gas sensors,⁵ flexible electronics and field emission devices,^{6,7} vertical interconnects for microelectronics,⁸ thermal interface materials and heat pipes,^{9–11} and unique optical absorbers.^{12,13} The unique morphology of VANTAs has been shown to be especially well suited for “gecko” type adhesives,^{14–16} supercompressible foams,¹⁷ and “carpets” from which fibers and transparent, conductive sheets can be continuously spun.^{18,19}

Two of the most important parameters governing the properties and applicability of VANTAs are their length and density. Understanding how to simultaneously monitor and control both the length and the density of VANTAs during growth by chemical vapor deposition (CVD) would enable the synthesis of constant-density VANTAs, VANTAs with tunable density, or more complex multilayered architectures tailored for particular properties. To measure and control the length of short VANTAs *in situ*, time-resolved optical reflectivity (TRR) has been demonstrated.²⁰ Direct measurements of VANTA height in real-time using TRR and imaging have been used to understand the growth kinetics of VANTAs, and even predict their ultimate length.^{20–23} For VANTAs $< 20 \mu\text{m}$ in length, TRR can control lengths with $\sim 20 \text{ nm}$ accuracy by simply terminating the constant feedstock gas flow after a

ABSTRACT The density of vertically aligned carbon nanotube arrays is shown to vary significantly during normal growth by chemical vapor deposition and respond rapidly to changes in feedstock flux. Pulsing the feedstock gas to repeatedly stop and start nanotube growth is shown to induce density variations up to a factor of 1.6 within *ca.* $1\text{--}2 \mu\text{m}$ long layers, allowing the synthesis of new array architectures with distinct regions of controllable length and density variation. Z-Contrast scanning transmission electron microscopy of corresponding sections of the arrays is used to provide unambiguous measurements of these density variations. Time-resolved optical reflectivity measurements of the height and optical extinction coefficient of the growing arrays are shown to provide a real-time diagnostic of both array density and growth kinetics.

KEYWORDS: carbon nanotube array · density · Z-STEM · pulsed CVD · *in situ* diagnostics · optical reflectivity

prescribed number of reflectivity oscillations.²⁰ However, similar *in situ* diagnostics and control over the density of VANTAs during growth have been lacking to date.

The density of VANTAs appears to be integrally linked to their growth mechanism, which is based on the cooperative growth of a nanotube forest from a high areal density of catalyst nanoparticles on a substrate. However, the mechanism by which nanotubes grow cooperatively to form a VANTA of uniform height is still not understood despite a number of interesting studies in this area.^{21–30} Only a fraction of available catalyst nanoparticles grow nanotubes and, due to variations in nanoparticle size and their interactions with the substrate, it is reasonable to expect that the nanoparticles which support nanotube growth have different catalytic activities, with some fraction capable of maintaining growth of a nanotube for a very long time under favorable conditions. Recent measurements of the mass density of arrays grown for different times have shown that just prior to the termination of array growth, the mass density decreases.³¹ This coincides with a progressive change in the apparent alignment

*Address correspondence to geohegandb@ornl.gov.

Received for review August 13, 2010 and accepted November 15, 2010.

Published online December 3, 2010.
10.1021/nn102029y

of the nanotubes from the top to the bottom of tall arrays as observed in SEM images, and as characterized by X-ray scattering and small-angle neutron scattering analyses.^{31–33} Thus it is reasonable to conclude that the termination of collective VANTA growth is attributable to a decrease in nanotube density below a critical threshold needed to maintain alignment.³¹ This density decrease has been attributed to Ostwald ripening, subsequent subsurface diffusion, or decreasing catalytic activity of the catalyst nanoparticles on the substrate.^{32,34} As a critical number of catalyst nanoparticles change shape, disappear, or become inactive, the cooperative growth of the array terminates.

Here we report the effects of changing feedstock gas flux on the growth of VANTAs, including those induced by “pulsed CVD”. Pulsing the feedstock gas at high flow velocity offers the opportunity to grow VANTAs “digitally” in predetermined *length* intervals by controlling the flux and duration of each pulse. VANTAs with precise heights might be fabricated by this procedure if growth can be reinitiated and continued from pulse to pulse. Rapid changes in feedstock gas flux during pulsed-CVD are shown to significantly change the *density* of the arrays over submicrometer lengths. Pulsed-CVD therefore offers the opportunity to tailor both the length and the density of VANTAs during different growth intervals to construct new multilayered array architectures with locally variable properties.

We describe our approach to extract both the evolution of height and density of growing VANTAs in real-time from TRR measurements.^{20,21} Differential changes in the optical extinction coefficient and the height of the arrays are used to estimate the changes in carbon density as the array adds new layers at the substrate by base growth. We show that the evolution of density derived from the *in situ* optical diagnostics agrees well with absolute measurements of the carbon density in the array determined by *ex situ* Z-contrast transmission electron microscopy (Z-STEM).

RESULTS AND DISCUSSION

In this study we use fast switching and pulsed delivery of CVD growth gases to explore fast, subsecond, nucleation and growth kinetics. In these experiments, similar substrates, catalysts, Ar/H₂/C₂H₂ gas mixture and flow rates were used as previously described.²¹ However, the flow velocity was increased 121-fold by lowering the pressure from 760 to 6.3 Torr, thereby decreasing the arrival time of the gas to the substrate from 26 to ~0.2 s.

For the pulsed growth of VANTAs, Ar and H₂ were flowed continuously and acetylene was injected “digitally” from electrically actuated valves either continuously or in discrete, well-separated pulses of ~0.2 s fwhm at the substrate. Each pulse was followed by typically 10 s of dead time to ensure growth had completed (as measured by TRR). The amount of gas and

the peak flux in each acetylene pulse could be varied by adjusting the acetylene pressure and the electrical pulse width applied to the valve. Thus, the kinetics of nucleation and growth resulting from each gas pulse can be measured separately using TRR, as discussed below. Detailed measurements of VANTA nucleation and growth kinetics enabled by this technique will be published elsewhere. Here we concentrate on the effects of pulsed gas injection on the density of the nanotube arrays.

Figure 1 shows the cross-section of a 114 μm tall VANTA with a multilayered architecture that was grown by pulsed CVD using 151 equal pulses of acetylene at 10 s intervals. The results of each pulse of gas are clearly seen as banded gradient zones in the array. TRR indicated that growth occurred within ~1 s for each pulse, so each band after the first corresponds to a separate, subsecond growth period. As the number of growth periods increase, the bandwidth decreases from 2.0 μm at the top of the array to 0.5 μm at the bottom most layer.

Figure 1b shows a magnified view of the first 11 growth segments from the top of the array, and Figure 1c shows the fourth and fifth bands, respectively. The magnified SEM images reveal that many vertically oriented nanotubes can be continuously traced across the interface between different growth bands. Additional disordered nanotubes, interwoven within the continuous, vertically oriented nanotubes, appear to comprise the brighter regions of the bands. These poorly aligned “crossbar” nanotubes grow during the early part of each renucleation and regrowth period.

By integrating the grayscale values within the dashed regions on the SEM micrographs plotted in yellow in Figures 1b,c, it is evident that each band in the images displays a gradient in intensity with peak intensities of measured secondary electrons corresponding to the early period of growth. Similar layering of VANTA structures has been observed when the gas flow was stopped or interrupted, resulting in disordered³⁵ or disconnected^{36,37} layers. In our experiments, the brighter regions in the SEM images correlate with the disordered regions of “crossbar” nanotubes that interweave with the more vertically aligned nanotubes which interconnect neighboring segments. Many different factors can affect the secondary electron emission yield and produce contrast variations in SEM images, including changing work function, changing conductivity, bundling of the nanotubes, or changing carbon density. As we will show below using Z-STEM, the origin of the contrast difference is most directly explained by the additional carbon density in the “crossbar” nanotube region.

Time-resolved reflectivity was employed to characterize the growth kinetics and optical properties of the VANTAs *in situ* during growth by pulsed CVD. The cross-section SEM image in Figure 2a shows the top 15 μm

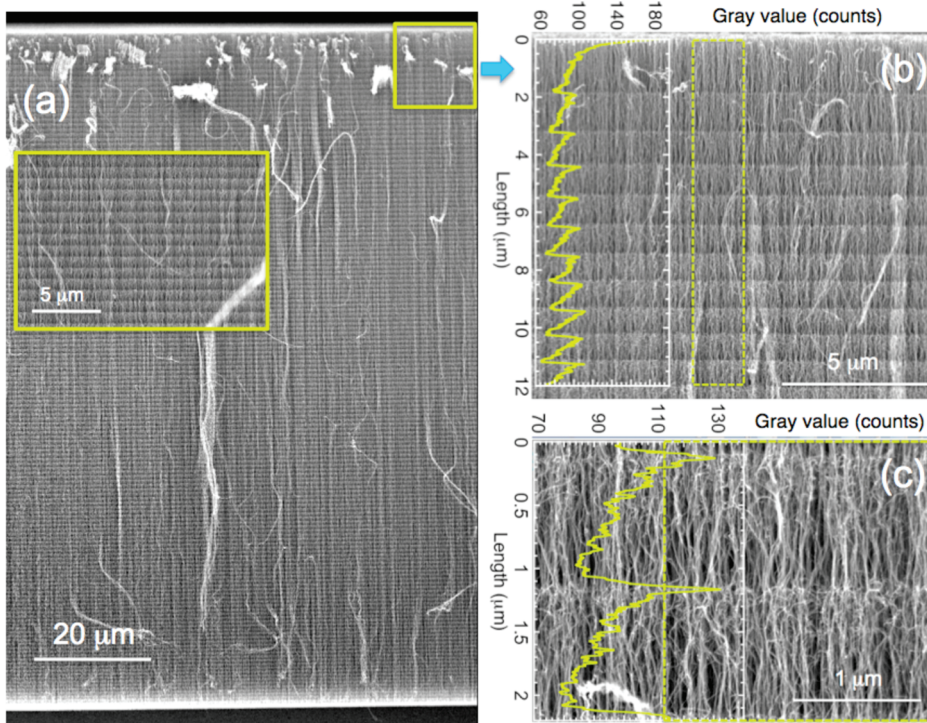


Figure 1. SEM cross-section images of a 114 μm tall multilayered VANTA architecture grown by pulsed CVD using 151 equal, discrete pulses of acetylene (est. peak flux of 576 sccm) into flowing Ar/H₂ at 690 °C and 6.3 Torr. (a) Cleaved array cross-section reveals bright bands marking the start of each new growth segment. (b) Magnified view of the first 11 layers of growth at the top of the array and overlaid integral of grayscale values within the dashed region quantifying the variation in contrast seen by eye. (c) Magnified view of two interfacial regions, showing a disordered layer of nanotubes interwoven into a forest of vertical nanotubes which appears continuous.

of a cleaved VANTA grown by pulsed CVD. The TRR signals which correspond to the first three gas pulses are shown in Figure 2b. In each case, the reflectivity signals show that the majority of growth occurs within 0.6 s. Each interference fringe in the TRR signals corresponds to 0.30 μm in length, so the 8, 6, and 5 interference

fringes measured for the first three gas pulses in Figure 2b correspond to predicted lengths of 2.4, 1.8, and 1.5 μm for the first three growth periods, respectively. Each nucleation and growth event leaves a distinct gradient band in the SEM images, with the brighter regions of the bands corresponding to the disordered layer of “crossbar” nanotubes forming during the early stages of growth. The lengths measured for each band in the cleaved array matched those predicted by TRR.

As shown in Figure 1a,b and Figure 2a, thin strips of the nanotube arrays were loosened by the cleavage process. These strips were carefully collected from the region corresponding to the optically monitored spot by gentle sonication in alcohol and deposited on lacey carbon TEM grids for analysis by SEM, TEM, and Z-STEM. The SEM and TEM measurements of the length of each band were checked against the original TRR growth record and the corresponding cross-section SEM measurements to ensure that compression or stretching of the arrays had not occurred.

Figure 3 panels a and b show TEM and Z-STEM images of the top three layers from a collected strip of the VANTA shown in Figure 2 and confirm that the nanotube array consists of two distinct components: nanotubes which appear to continuously interconnect throughout the array, and randomly oriented nanotubes which appear only during the high flux portion of each new gas pulse to form entangled “crossbars”.

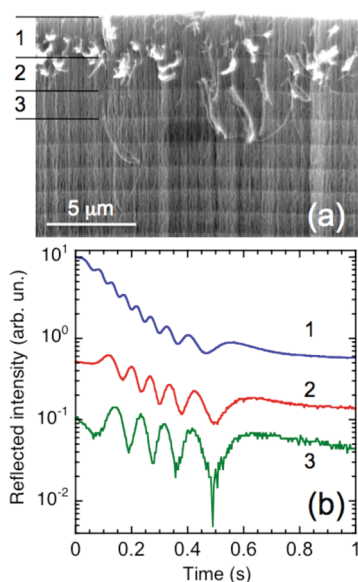


Figure 2. (a) A cross-section SEM image of a VANTA grown using subsecond exposures of acetylene into fast-flowing Ar/H₂ at 10 s intervals. (b) The reflected laser (633 nm) intensity vs time for the first three gas pulses.

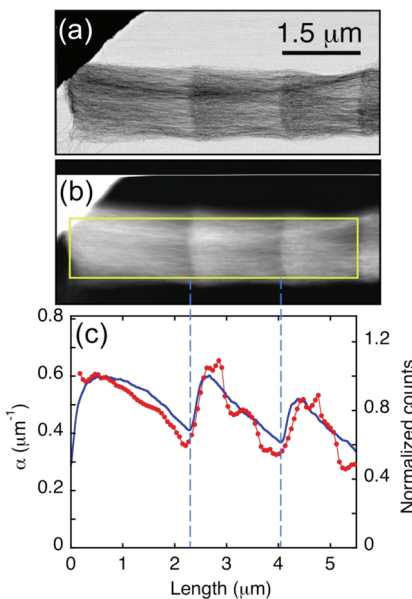


Figure 3. (a) TEM and (b) Z-STEM images of a VANTA grown by pulsed C_2H_2 gas introduction. (c) Extinction coefficient derived from real-time TRR measurements (connected dots) and Z-STEM image intensity distribution along the VANTA length (solid curve) binned inside the rectangle shown in panel b.

Z-STEM image analysis is a reliable technique used to quantify the density of materials such as biomolecules.^{38–40} In these experiments Z-STEM was used to unambiguously provide a direct measure of carbon density vs length in samples of the VANTAs. The intensity of the Z-STEM image is directly proportional to the mass of carbon that the electron beam traverses (see Methods section) with the brighter regions of the image corresponding to higher carbon densities. By integrating the counts in the Z-STEM image intensity within the rectangular area shown in Figure 3b, the blue curve in Figure 3c is obtained, which represents the relative variation in carbon density along the VANTA length. The carbon density in the VANTA exhibits a pronounced variation (up to a factor of 1.6) over the period of each gas pulse. The density peaks during the high-flux, fast-growth region of each growth period, and then declines during the low-flux tail of each pulse. The peak in density occurs within the region of disordered “crossbar” nanotubes which grow during the nucleation and early growth period of each gas pulse.

The red points in Figure 3c are estimates of the optical extinction coefficient for each corresponding position in the array derived from the *in situ* TRR measurements shown in Figure 2b. A central result of this work is the remarkable agreement (<24% difference) between the variation in the normalized optical extinction coefficient and the carbon density changes determined from Z-STEM images (blue line). The shape of the interference fringes and the attenuation of the reflected intensity in each growth region provide a record of the evolution in length from the top surface of the

VANTA, $d(t)$, and the corresponding optical characteristics in that region, which are described by an effective complex refractive index, $\tilde{n}_b(d) = n_b(d) + ik_b(d)$.^{20,21} Two fitting methods were considered to obtain the optical constants vs length from the TRR signal: a complete fit of the measured reflectivity curves (see Methods section) and an approximate procedure.

In the approximate procedure, the goal is simply to extract the local exponential attenuation of the oscillating reflectivity signal to obtain the effective extinction coefficient for each region. First, the reflectivities of the oscillation maxima $R(N_{\max})$ and minima $R(N_{\min})$ in Figure 2b are recorded (see Supporting Information Figure S1). Then, the resulting dependences are linearly interpolated, then averaged and plotted to obtain an averaged curve of reflectivity vs fringe number, $R(N)$, from which the effective extinction coefficient is derived as

$$\alpha = -\frac{d[\ln(R/R_0)]}{d(2d_0N)}$$

The effective extinction coefficient obtained by this procedure exhibits periodic variations with length that closely follow the density profile measured by Z-STEM intensity analysis in Figure 3c. In addition to the periodic behavior, both the measured carbon density and the effective extinction coefficient exhibit a gradual decline with length, $d = d_0N$, for increasing number of pulses. However, the effective optical extinction coefficient exhibits interesting secondary structure that does not appear in the measured carbon density profile. Estimates of variations in the extinction coefficient introduced by the interpolation process in the approximate procedure could not account for the magnitude of this secondary structure, and may result from changing the alignment of some fraction of nanotubes at particular positions inside the array. It is well-known that optical absorption cross sections are sensitive to the alignment of the nanotubes with the light polarization axis. Nanotubes oriented parallel to the polarization axis absorb more strongly than those that are perpendicular. Since the effective optical extinction coefficient $\alpha = \rho\sigma$, where ρ is the density of the VANTA layer and σ is its effective extinction cross-section, the overall good agreement between the measured optical extinction coefficient and density implies a relatively weak dependence of the effective extinction cross section on variations in VANTA characteristics or orientation.

In addition to possible changes in nanotube alignment within the array, other characteristics of the VANTA may change during growth. The distributions of nanotube diameters, wall-numbers, and fraction of non-nanotube carbon may change due to changing catalytic activity, temperature, flux, or growth rate.^{21,22,41} Each of these factors may affect the optical extinction coefficient. Over the approximately mm laser beam

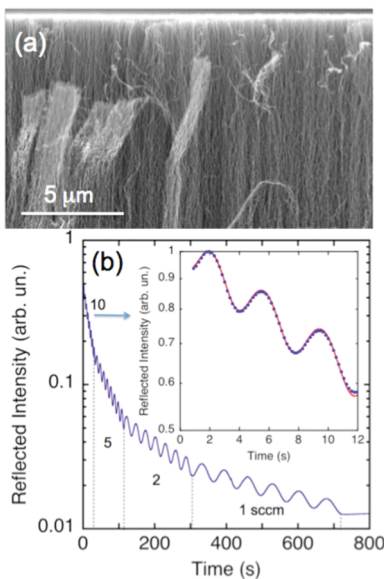


Figure 4. (a) SEM cross-section image of a cleaved VANTA array grown at 690 °C using an Ar/H₂/C₂H₂ gas mixture at 6.3 Torr. The C₂H₂ flow rate was smoothly changed three times during growth. (b) Intensity of the reflected HeNe laser beam *vs* growth time. The growth starts at *t* = 0 and the vertical dotted lines show the times when acetylene flow is switched from 10 to 5; 5 to 2; and 2 to 1 sccm, respectively. The inset shows an example of a complete fit to the experimental curve (dots) using eq 1 in the Methods section.

spot used for TRR, the vinelike morphology of billions of nanotubes in the VANTA present a multitude of three-dimensional orientations, so the effective extinction cross-section for a layer represents an average which accounts for the multitude of orientations in the VANTA layer and the effects of these additional factors.

Nanotube arrays grown with continuous gas introduction showed similar magnitudes of decline in extinction coefficient and density, without the presence of “crossbar” nanotubes or visible bands in the SEM images. Figure 4a shows a cross-section SEM image of a VANTA grown when the flow rate of the continuously injected feedstock gas was smoothly switched during the growth from 10 sccm, to 5, to 2, and finally to 1 sccm. Unlike the SEM images of Figures 1 and 2, no banded regions are apparent to easily interpret the growth regions. The corresponding *in situ* TRR measurements are shown in Figure 4b. Below we describe how the length and optical extinction coefficient of each VANTA region is extracted from the corresponding fringe spacings and the exponential decay in the TRR signal.

The inset in Figure 4b shows a three-fringe segment of the 10-sccm portion of the reflectivity curve and a fit to the data using the complete fit procedure described in the Methods section. As indicated by the excellent fit in this example, a fit to three fringes of growth (~ 900 nm) was found to best determine the fit parameters within that length and time region. The time dependence of the fit parameters was obtained

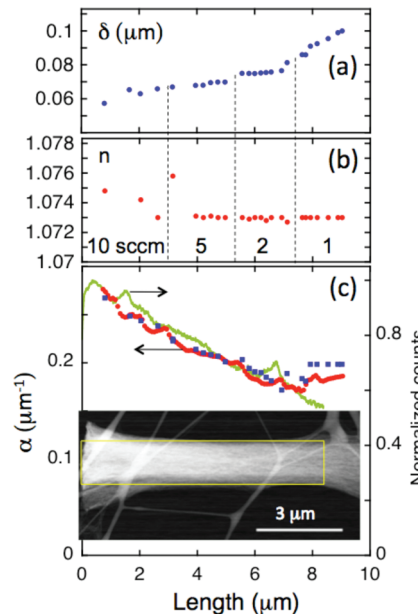


Figure 5. (a) Roughness, (b) refractive index, and (c) extinction coefficient (blue squares) *vs* the length of the VANTA derived from a complete fit of the experimental reflectivity curves in Figure 4 to eq 1 (Methods section). The red solid circles in panel c show α obtained using a simplified procedure (see text) compared to the full regression analysis (blue). The inset at the bottom shows a Z-STEM image of the corresponding top region of the VANTA in Figure 4a. The normalized Z-STEM image intensity integrated *vs* VANTA length within the indicated area is plotted (green curve in panel c) as a direct measure of the density variation. Contributions to the measured carbon density from the lacey carbon grid supports are evident as small peaks at the corresponding positions on this curve.

by rolling fits of three-fringe regions as each new fringe could be discerned.

Figure 5 shows the resulting optical parameters as a function of length of the nanotube array for a series of such fits. The most notable change is a factor of 1.6 change in the effective extinction coefficient $\alpha = 4\pi k_b/\lambda$ of the VANTA which decreases from $0.28 \mu\text{m}^{-1}$ to $\sim 0.17 \mu\text{m}^{-1}$ over the 9 μm length. Similar variations occur for arrays grown using constant feedstock flows (see Supporting Information, Figure S2). In addition, Figure 5b shows that the complete fit to the data indicates that the roughness of the top VANTA layer δ increases from ~ 60 to ~ 100 nm as the array grows to 9 μm length. Although the top VANTA layer is formed early in the growth process, *in situ* imaging has revealed that its roughness can continue to evolve late in the growth process,²³ presumably from internal stresses inherent to the coordinated growth mechanism of the array. However, the effective refractive index n of the array given in Figure 5b does not change appreciably over the length.

Also shown in Figure 5c are the estimates of the extinction coefficient from the simplified data analysis approach described previously. Although this approximate procedure essentially neglects the contributions to the reflected signal from multiple internal reflections

within the array (second term in the denominator of eq 1, Methods section) and also the nearly constant reflected signal from the rough, top layer (the first term in eq 1), in most cases, as in Figure 5c, the extinction coefficient obtained using this approach matches well with that derived through the nonlinear least-squares fit of the complete reflectivity curve. Both the complete and approximate fit procedures indicate that the optical extinction coefficient of the array decreases significantly with length as the VANTA grows.

Z-STEM image intensity analysis of a sample of the array (shown in the inset to Figure 5c) was again used to directly measure the variation in VANTA density along its length. The carbon density given by the green curve in Figure 5c also decreased by a factor of 1.6 during the first 8.5 μm of growth, following the same trend as the extinction coefficient derived from the *in situ* optical measurements. The excellent agreement between the carbon density variations measured by Z-STEM and the optical extinction coefficient variations measured by TRR for both pulsed growth and continuous growth of VANTAs validates TRR as an effective *in situ* diagnostic tool for determining the density variations within growing nanotube arrays.

The decline in the extinction coefficient during growth by continuous feedstock introduction cannot be explained solely by changes in nanotube alignment with array length. Millimeters-long VANTAs grown with continuous feedstock gas introduction have been shown to develop pronounced orientation changes which have been characterized by small-angle X-ray scattering and small-angle neutron scattering.^{32,33} However, SEM and TEM imaging show that for the relatively short array lengths ($<20 \mu\text{m}$) which were optically monitored in these continuous flow studies, no nanotube alignment changes could be discerned.

Different interpretations have been proposed to explain observations of long-term declines in the density of VANTAs and the eventual termination of their collective growth during CVD. These include Ostwald ripening,²⁶ poisoning, and overcoating of the catalyst nanoparticles. In these models, the overall number of active catalyst nanoparticles is reduced by different mechanisms. To minimize Ostwald ripening of the catalyst in these experiments, all catalyst films underwent a 5–10 min annealing period at the growth temperature in Ar/H₂ flow prior to growth during which time the TRR signal was stable. Nevertheless, the densities of arrays grown under different constant feedstock fluxes tended to monotonically decline.

According to a simplified rate equation-based model developed to describe the observed growth kinetics during the sustained growth of long VANTAs,^{21,22} catalyst nanoparticles assist in multiple functions, with different rates for cracking of the feedstock gas to introduce carbon on the surface of a nanoparticle, diffusion of the surface (or subsurface) carbon to an active site,

and incorporation of the carbon into a nanotube. In the model, buildup of amorphous carbon on the nanoparticle surface restricts its effective surface area (and represents many possible means of catalyst deactivation) ultimately leading to the termination of growth. Conversely, dissolution or chemical etching of this surface carbon (e.g., by hydrogen) represents a means of catalyst recovery. The pulsed CVD results indicate that a high density of catalyst sites can be reactivated despite this apparent long-term decline in site density. If one assumes that the coordinated growth of VANTAs relies upon a cooperative adjustment in the catalytic activities of nanoparticles within an ensemble, then introducing transients in the gas flux permits a way to re-examine this cooperative adjustment of the nanoparticle ensemble at different phases in the growth of the VANTA. The nonequilibrium nature of the pulsed growth process, with periods of growth at high feedstock flux followed by periods of recovery with only Ar/H₂ flow, represents a promising avenue for reactivation of catalyst site density.

Considering the pulsed growth results in the context of this model, nanotubes should initially grow from all catalyst nanoparticles during each new gas pulse; however, only some nanoparticles should have catalytic rates that are balanced to sustain growth throughout the duration of the pulse without overcoating. However, the recovery time between pulses (10 s in these experiments) is sufficient for some deactivated catalyst nanoparticles to have a chance to recover their activity. Thus, the nonequilibrium processes occurring in a periodic growth gas supply appear to repeatedly reactivate nanoparticles, initiate growth from a high density of available sites, and downselect those with sufficiently broad tolerance to deactivation, producing VANTAs with periodically changing density.

CONCLUSIONS

Time-resolved optical reflectivity measurements of the height and optical extinction coefficient of VANTAs during growth have been shown to provide a real-time diagnostic of both growth kinetics and array density. The rapid density variations induced by pulsed growth provide a pathway for digital synthesis of new variable-density VANTA architectures. Through variation of the pulsed flux and duration, the lengths and densities of each region can be adjusted, which provides opportunities to tune the thermal, optical, acoustic, and electromagnetic properties of VANTAs.

The ability to measure the variation of density *in situ* during growth, coupled with the rapid variations induced by pulsing the feedstock flux, lead to several new conclusions about the cooperative growth of nanotubes in VANTAs. First, the densities of the arrays are flux dependent, and the growth process is capable of responding to rapid flux variations. As shown above, VANTAs can nucleate and grow

micrometers in length during subsecond periods. During this time, the VANTA density can vary by a factor of at least 1.6 with higher density regions corresponding to the periods of high flux.

Second, a decline in density is noted in the growth of arrays (e.g., Figure 5) with constant feedstock flux. In both continuous and pulsed growth, the measurement of growth rate and density indicate a gradual decline in catalytic activity. This decline has been attributed to various phenomena such as Ostwald ripening, poisoning, or overcoating of the catalyst. While each of these mechanisms undoubtedly occurs to a degree, the ability of the nanoparticle ensemble to repeatedly renucleate and regrow high densities of nanotubes with successive pulses of feedstock indicates that pulsing the

flux can provide the conditions to reactivate sites for nanotube growth that would otherwise remain inactive under a given flow condition.

The ability to digitally vary the duration and flux of gas, coupled with the development of real-time *in situ* diagnostics of both VANTA density and growth rate, affords new opportunities to understand the flux dependence of nucleation (and renucleation) kinetics, effects on the diameter and wall number distributions of the nanotubes, and details of the cooperative growth phenomena which will be presented in a separate publication. Moreover, these diagnostics afford the pathway to optimize advanced nanotube architectures with variable length and anisotropic density distributions for a variety of applications.

METHODS

CVD Growth of VANTAs. Ar/H₂/C₂H₂ gas mixtures were introduced into a 3''-diameter, 4'-long quartz tube-furnace reactor as previously described²¹ except that the pressure was lowered from 760 to 6.3 Torr, thereby decreasing the arrival time of the gas to the substrate from 26 to ~0.2 s, and increasing the flow velocity 121 fold. Si(100) wafer substrates were coated with catalyst bilayers with nominal thickness of 0.5 nm Fe and 30 nm Al₂O₃.

Pulsed CVD Growth. For pulsed growth, Ar (2000 sccm) and H₂ (250 sccm) gases were flowed continuously and acetylene gas was injected "digitally" from a pulsed valve (Parker model: 099-0167-900) which was electrically actuated by a circuit which was electrically triggered by a digital delay generator (Stanford Research Systems, SR545). The pulsed valve could be opened for minimum times of 1 ms, then closed, producing ~0.2 s fwhm pulses of acetylene at the substrate. Each pulse was followed by typically 10s of time to ensure growth had completed (as measured by TRR). The amount of gas and the peak acetylene flux in each pulse were varied by adjusting the backing gas pressure of acetylene to the valve and the gate width of the applied electrical pulse.

Time-Resolved Reflectivity. The intensity of the HeNe laser beam reflected from the vertically standing substrate was monitored using a Si photodiode with a 633 nm interference filter.^{20,21} The photocurrent was conditioned with a transimpedance amplifier (gain 1 V/10 μA), digitized with a LabJack 12-bit A/D converter at 300 samples/s, and computer recorded.

Reflectivity Data Analysis. To analyze the experimental reflectivity curves shown in Figure 4b, we used the following complete fit procedure. The shape of the interference fringes and the attenuation of the reflected intensity in each growth region (Figure 4b) are determined by the evolution in length, $d(t)$, of the VANTA and its optical characteristics, which are described by an effective complex refractive index, $\bar{n}_b = n_b + ik_b$.^{20,21} In the complete fit of the curves, we follow the well-established notation of an effective medium model, considering three layers: (a) Ar/H₂/C₂H₂, $n_a = 1$; (b) VANTAs, $\bar{n}_b = n_b + ik_b$; and (c) Si, $\bar{n}_c = 4.1 + 0.057i$.²¹

Here the complex reflective amplitude, r_{ab} , is modified from that in ref 21, eq 2 to include scattering effects induced from roughness on the top layer of the VANTA:⁴²

$$r_{ab} = \rho_{ab} S_{\text{ext}} + \frac{S_t^2 \tau_{ab} \rho_{bc} \Phi^2}{1 - S_{\text{int}} \rho_{bc} \rho_{ba} \Phi^2} \quad (1)$$

where δ , the roughness of the top VANTA layer, is introduced in three scattering factors:

$$\begin{aligned} S_{\text{ext}} &= \exp\left[-\frac{1}{2}\left(\frac{4\pi\delta}{\lambda}\right)^2\right] \\ S_{\text{int}} &= \exp\left[-\frac{1}{2}\left(\frac{4\pi n_b \delta}{\lambda}\right)^2\right] \\ S_t &= \exp\left[-\frac{1}{2}\left(\frac{2\pi(n_b - 1)\delta}{\lambda}\right)^2\right] \end{aligned} \quad (2)$$

which, respectively, correspond to external backscattering of the incoming beam from the rough top VANTA surface back into the surrounding gas, scattering encountered during transmission of the beam through the rough top layer into the VANTA, and internal scattering off the rough interface from backscattered beams within the VANTA. The effects of including roughness in the model is assessed for $\lambda = 632.8$ nm.

For normal incidence, the amplitude reflection and transmission coefficients at each interface, ρ_{ij} and τ_{ij} , are defined as

$$\rho_{ij} = \frac{\bar{n}_i - \bar{n}_j}{\bar{n}_i + \bar{n}_j}, \quad \tau_{ij} = \frac{2\bar{n}_i}{\bar{n}_i + \bar{n}_j} \quad (3)$$

where $i, j = a, b, c$ and $\Phi = \exp(i2\pi\bar{n}_b d(t)/\lambda)$ is the phase factor at normal incidence.⁴³ Therefore, predicted reflectivity curves are calculated as $R(t) = r_{ab}^* r_{ab}$ and must be fit to the experimental data to obtain $d(t)$, and corresponding values for \bar{n}_b and δ .

To regressively fit the experimental reflectivity curves, initial values for $d(t)$ were obtained by fixing the real part of the total refractive index, \bar{n}_b , as a constant across the VANTA length. In this case the VANTA lengths at times corresponding to the maxima and minima of the oscillations can be obtained simply by counting the number of fringes at the corresponding times, using $N(t_{\max}) = 0, 1, 2, \dots$ and $N(t_{\min}) = 0, 0.5, 1.5, 2.5, \dots$:

$$d(t_{\max}) = N(t_{\max})d_0, \quad d(t_{\min}) = N(t_{\min})d_0 \quad (4)$$

where $d_0 = \lambda/(2n_b)$, the length per fringe in the case of normal incidence,²¹ was determined experimentally by measuring the length of cross-sectioned VANTAs by electron microscopy when the growth was intentionally stopped after specific numbers of fringes.^{20,21} Having calibrated the lengths corresponding to the peaks and valleys of the fringes, the height of the VANTA at any time $d(t)$ could be obtained using a cubic polynomial fit to either the discrete $d(t_{\max})$ or $d(t_{\min})$ data points

$$d(t) = c_0 + c_1 t + c_2 t^2 + c_3 t^3 \quad (5)$$

where the c_0, c_1, c_2 , and c_3 are the corresponding fitting parameters.

These parameters were used as starting values for a nonlinear least-squares fit of $d(t)$, $\delta(d)$, $n_b(d)$ and $\alpha(d)$ using Matlab and the Levenberg–Marquardt algorithm.

Z-STEM Image Analysis of Density. TEM and Z-STEM methods were developed and used extensively to determine masses of biomolecules.^{39–41} The Z-STEM technique employed here is based on collecting electrons elastically scattered onto an annular detector of a Hitachi HD-2000 microscope operating at 200 kV. The molecular mass of VANTAs can be determined as⁴¹

$$M = Nm = \frac{IAm}{I_0[\sigma_e + \sigma_i]} \quad (6)$$

where m and N are the atomic mass and the total number of carbon atoms within the pixel area A , respectively, I/I_0 is the fraction of the incident electron beam, I_0 , deflected toward the annular detector, and σ_e and σ_i are the elastic and inelastic scattering cross sections, respectively. Here we also assume that a relatively thin layer of a carbon nanotube array is monitored with an electron beam. The relative intensity of the deflected electron beam was determined based on the Z-STEM image intensities recorded by the microscope's CCD camera. The contrast of the image was adjusted to keep the signal from saturating within an 8-bit range, and the brightness of the image was adjusted so that the darkest part of the image, with the electron beam blocked, still had a few positive counts.

Acknowledgment. Research was sponsored by the Materials Sciences and Engineering Division, Office of Basic Energy Sciences, U.S. Department of Energy. Z-STEM measurement of nanotube density was conducted at the Center for Nanophase Materials Sciences, and HRTEM was performed in the Shared Research Equipment User Facility, which are sponsored at Oak Ridge National Laboratory by the Scientific User Facilities Division, U.S. Department of Energy. We gratefully acknowledge David Joy for help with microscopy estimations of densities.

Supporting Information Available: Time-resolved reflectivity data and optical extinction coefficient evolution for VANTAs grown with constant feedstock flux, illustration of the approximate fitting procedure to estimate optical extinction coefficients from time-resolved reflectivity data. This material is available free of charge via the Internet at <http://pubs.acs.org>.

REFERENCES AND NOTES

- Dresselhaus, M. S.; Dresselhaus, G.; Avouris, P., Eds. *Carbon Nanotubes: Synthesis, Structure, Properties, and Applications*. Springer: Berlin, 2001; Vol. 80.
- Baughman, R. H.; Zakhidov, A. A.; de Heer, W. A. Carbon Nanotubes—The Route Toward Applications. *Science* **2002**, *297*, 787–792.
- Endo, M.; Strano, M. S.; Ajayan, P. M. Potential Applications of Carbon Nanotubes. *Top. Appl. Phys.* **2008**, *111*, 13–61.
- Rouleau, C. M.; Eres, G.; Cui, H.; Christen, H. M.; Puretzky, A. A.; Geohegan, D. B. Altering the Catalytic Activity of Thin Metal Catalyst Films for Controlled Growth of Chemical Vapor Deposited Vertically Aligned Carbon Nanotube Arrays. *Appl. Phys. A* **2008**, *93*, 1005–1009.
- Modi, A.; Koratkar, N.; Lass, E.; Wei, B. Q.; Ajayan, P. M. Miniaturized Gas Ionization Sensors Using Carbon Nanotubes. *Nature* **2003**, *424*, 171–174.
- Pint, C. L.; Xu, Y. Q.; Pasquali, M.; Hauge, R. H. Formation of Highly Dense, Aligned Ribbons and Transparent Films of Single-Walled Carbon Nanotubes Directly from Carpets. *ACS Nano* **2008**, *2*, 1871–1878.
- Tsai, T. Y.; Lee, C. Y.; Tai, N. H.; Tuan, W. H. Transfer of Patterned Vertically Aligned Carbon Nanotubes Onto Plastic Substrates for Flexible Electronics and Field Emission Devices. *Appl. Phys. Lett.* **2009**, *95*, 013107.
- Awano, Y.; Sato, S.; Kondo, D.; Ohfuti, M.; Kawabata, A.; Nihei, M.; Yokoyama, N. Carbon Nanotube via Interconnect Technologies: Size-Classified Catalyst Nanoparticles and Low-Resistance Ohmic Contact Formation. *Phys. Status Solidi A* **2006**, *203*, 3611–3616.
- Ivanov, I.; Puretzky, A.; Eres, G.; Wang, H.; Pan, Z. W.; Cui, H. T.; Jin, R. Y.; Howe, J.; Geohegan, D. B. Fast and Highly Anisotropic Thermal Transport Through Vertically Aligned Carbon Nanotube Arrays. *Appl. Phys. Lett.* **2006**, *89*, 223110.
- Hu, X. J.; Padilla, A. A.; Xu, J.; Fisher, T. S.; Goodson, K. E. 3-Omega Measurements of Vertically Oriented Carbon Nanotubes on Silicon. *J. Heat Trans.* **2006**, *128*, 1109–1113.
- Akoshima, M.; Hata, K.; Futaba, D. N.; Mizuno, K.; Baba, T.; Yumura, M. Thermal Diffusivity of Single-Walled Carbon Nanotube Forest Measured by Laser Flash Method. *Jpn. J. Appl. Phys.* **2009**, *48*, 05EC07.
- Yang, Z. P.; Ci, L. J.; Bur, J. A.; Lin, S. Y.; Ajayan, P. M. Experimental Observation of an Extremely Dark Material Made by a Low-Density Nanotube Array. *Nano Lett.* **2008**, *8*, 446–451.
- Mizuno, K.; Ishii, J.; Kishida, H.; Hayamizu, Y.; Yasuda, S.; Futaba, D. N.; Yumura, M.; Hata, K. A Black Body Absorber from Vertically Aligned Single-Walled Carbon Nanotubes. *Proc. Natl. Acad. Sci. U.S.A.* **2009**, *106*, 6044–6047.
- Ge, L.; Sethi, S.; Ci, L.; Ajayan, P. M.; Dhinojwala, A. Carbon Nanotube-Based Synthetic Gecko Tapes. *Proc. Natl. Acad. Sci. U.S.A.* **2007**, *104*, 10792–10795.
- Qu, L.; Dai, L. Gecko-Foot-Mimetic Aligned Single-Walled Carbon Nanotube Dry Adhesives with Unique Electrical and Thermal Properties. *Adv. Mater.* **2007**, *19*, 3844.
- Qu, L. T.; Dai, L. M.; Stone, M.; Xia, Z. H.; Wang, Z. L. Carbon Nanotube Arrays with Strong Shear Binding-On and Easy Normal Lifting-Off. *Science* **2008**, *322*, 238–242.
- Cao, A. Y.; Dickrell, P. L.; Sawyer, W. G.; Ghasemi-Nejhad, M. N.; Ajayan, P. M. Supercompressible Foamlike Carbon Nanotube Films. *Science* **2005**, *310*, 1307–1310.
- Zhang, M.; Atkinson, K. R.; Baughman, R. H. Multifunctional Carbon Nanotube Yarns by Downsizing an Ancient Technology. *Science* **2004**, *306*, 1358–1361.
- Peng, H. S.; Jain, M.; Li, Q. W.; Peterson, D. E.; Zhu, Y. T.; Jia, Q. X. Vertically Aligned Pearl-like Carbon Nanotube Arrays for Fiber Spinning. *J. Am. Chem. Soc.* **2008**, *130*, 1130.
- Geohegan, D. B.; Puretzky, A. A.; Ivanov, I. N.; Jesse, S.; Eres, G.; Howe, J. Y. *In Situ* Growth Rate Measurements and Length Control During Chemical Vapor Deposition of Vertically Aligned Multiwall Carbon Nanotubes. *Appl. Phys. Lett.* **2003**, *83*, 1851–1853.
- Puretzky, A. A.; Geohegan, D. B.; Jesse, S.; Ivanov, I. N.; Eres, G. *In Situ* Measurements and Modeling of Carbon Nanotube Array Growth Kinetics During Chemical Vapor Deposition. *Appl. Phys. A* **2005**, *81*, 223–240.
- Wood, R. F.; Pannala, S.; Wells, J. C.; Puretzky, A. A.; Geohegan, D. B. Simple Model of the Interrelation between Single- and Multiwall Carbon Nanotube Growth Rates for the CVD Process. *Phys. Rev. B* **2007**, *75*, 235446.
- Puretzky, A. A.; Eres, G.; Rouleau, C. M.; Ivanov, I. N.; Geohegan, D. B. Real-Time Imaging of Vertically Aligned Carbon Nanotube Array Growth Kinetics. *Nanotechnology* **2008**, *19*, 055605.
- Meshot, E. R.; Hart, A. J. Abrupt Self-Termination of Vertically Aligned Carbon Nanotube Growth. *Appl. Phys. Lett.* **2008**, *92*, 113107.
- Nessim, G. D.; Seita, M.; O'Brien, K. P.; Hart, A. J.; Bonaparte, R. K.; Mitchell, R. R.; Thompson, C. V. Low Temperature Synthesis of Vertically Aligned Carbon Nanotubes with Electrical Contact to Metallic Substrates Enabled by Thermal Decomposition of the Carbon Feedstock. *Nano Lett.* **2009**, *9*, 3398–3405.
- Amama, P. B.; Pint, C. L.; McJilton, L.; Kim, S. M.; Stach, E. A.; Murray, P. T.; Hauge, R. H.; Maruyama, B. Role of Water in Super Growth of Single-Walled Carbon Nanotube Carpets. *Nano Lett.* **2009**, *9*, 44–49.
- Pint, C. L.; Pheasant, S. T.; Parra-Vasquez, A. N. G.; Horton, C.; Xu, Y. Q.; Hauge, R. H. Investigation of Optimal Parameters for Oxide-Assisted Growth of Vertically Aligned Single-Walled Carbon Nanotubes. *J. Phys. Chem. C* **2009**, *113*, 4125–4133.
- Wirth, C. T.; Zhang, C.; Zhong, G. F.; Hofmann, S.; Robertson, J. Diffusion- and Reaction-Limited Growth of Carbon Nanotube Forests. *ACS Nano* **2009**, *3*, 3560–3566.
- Eres, G.; Rouleau, C. M.; Yoon, M.; Puretzky, A. A.; Jackson,

- J. J.; Geohegan, D. B. Model for Self-Assembly of Carbon Nanotubes from Acetylene Based on Real-Time Studies of Vertically Aligned Growth Kinetics. *J. Phys. Chem. C* **2009**, *113*, 15484–15491.
30. Vinten, P.; Marshall, P.; Lefebvre, J.; Finnie, P. Distinct Termination Morphologies for Vertically Aligned Carbon Nanotube Forests. *Nanotechnology* **2010**, *21*, 035603.
31. Bedewy, M.; Meshot, E. R.; Guo, H.; Verploegen, E. A.; Lu, W.; Hart, A. J. Collective Mechanism for the Evolution and Self-Termination of Vertically Aligned Carbon Nanotube Growth. *J. Phys. Chem. C* **2009**, *113*, 20576–20582.
32. Wang, B. N.; Bennett, R. D.; Verploegen, E.; Hart, A. J.; Cohen, R. E. Quantitative Characterization of the Morphology of Multiwall Carbon Nanotube Films by Small-Angle X-ray Scattering. *J. Phys. Chem. C* **2007**, *111*, 5859–5865.
33. Wang, H.; Xu, Z.; Eres, G. Order in Vertically Aligned Carbon Nanotube Arrays. *Appl. Phys. Lett.* **2006**, *88*, 213111.
34. Kim, S. M.; Pint, C. L.; Amama, P. B.; Zakharov, D. N.; Hauge, R. H.; Maruyama, B.; Stach, E. A. Evolution in Catalyst Morphology Leads to Carbon Nanotube Growth Termination. *J. Phys. Chem. Lett.* **2010**, *1*, 918.
35. Liu, K.; Jiang, K. L.; Feng, C.; Chen, Z.; Fan, S. S. A Growth Mark Method for Studying Growth Mechanism of Carbon Nanotube Arrays. *Carbon* **2005**, *43*, 2850–2856.
36. Li, X. S.; Cao, A. Y.; Jung, Y. J.; Vajtai, R.; Ajayan, P. M. Bottom-Up Growth of Carbon Nanotube Multilayers: Unprecedented Growth. *Nano Lett.* **2005**, *5*, 1997–2000.
37. Iwasaki, T.; Robertson, J.; Kawarada, H. Mechanism Analysis of Interrupted Growth of Single-Walled Carbon Nanotube Arrays. *Nano Lett.* **2008**, *8*, 886–890.
38. Burge, R. E.; Silvester, N. R. The Measurement of Mass, Thickness, and Density in the Electron Microscope. *J. Biophys. Biochem. Cytol.* **1960**, *8*, 1–11.
39. Muller, S. A.; Engel, A. Structure and Mass Analysis by Scanning Transmission Electron Microscopy. *Micron* **2001**, *32*, 21–31.
40. Sousa, A. A.; Leapman, R. D. Quantitative STEM Mass Measurement of Biological Macromolecules in a 300 kV TEM. *J. Microsc.* **2007**, *228*, 25–33.
41. Feng, X.; Liu, K.; Xie, X.; Zhou, R.; Zhang, L.; Li, Q.; Fan, S.; Jiang, K. Thermal Analysis Study of the Growth Kinetics of Carbon Nanotubes and Epitaxial Graphene Layers on Them. *J. Phys. Chem. C* **2009**, *113*, 9623–9631.
42. Choi, S.; Lee, S.; Koh, K. H. *In Situ* Optical Investigation of Carbon Nanotube Growth in Hot-Filament Chemical Vapor Deposition. *Curr. Appl. Phys.* **2006**, *6*, e38–e42.
43. Theiss, W. Optical Properties of Porous Silicon. *Surf. Sci. Rep.* **1997**, *29*, 95–192.